



NOVA

University of Newcastle Research Online

nova.newcastle.edu.au

Mirzaeva, Galina; Goodwin, Graham "Current control with improved tracking and harmonic performance for a voltage source inverter driving a saturated induction motor". Originally published in Proceedings of the 2016 International Symposium on Power Electronics, Electrical Drives, Automation and Motion (SPEEDAM 2016) (Anacapri, Italy 22-24 June, 2016) p. 709-714 (2016)

Available from: <http://dx.doi.org/10.1109/SPEEDAM.2016.7525891>

© 2016 IEEE. Personal use of this material is permitted. Permission from IEEE must be obtained for all other uses, in any current or future media, including reprinting/republishing this material for advertising or promotional purposes, creating new collective works, for resale or redistribution to servers or lists, or reuse of any copyrighted component of this work in other works.

Accessed from: <http://hdl.handle.net/1959.13/1325572>

Current Control with Improved Tracking and Harmonic Performance for a Voltage Source Inverter Driving a Saturated Induction Motor

Abstract—Magnetic saturation in induction motors is a very common, complex and undesirable phenomenon. It reduces the accuracy of drive control with respect to the fundamental current/voltage components, and gives rise to additional harmonics which degrades the total harmonic performance of the drive. The existing mitigation strategies include accurate modeling of the saturated motor and harmonic filtering. A different approach is presented in this paper. An advanced control scheme is designed which specifically targets and eliminates the tracking error at fundamental frequency and harmonic components produced by magnetic saturation. The paper includes theoretical development of the control scheme by utilizing general Model Predictive Control (MPC) framework. It also discusses and addresses various aspects of practical implementation. The findings of the paper are illustrated by extensive simulation and provisional experimental results.

I. INTRODUCTION

Magnetic saturation in induction motors is a known and well-studied phenomenon. Similar to other devices utilizing magnetic materials, induction motors are designed to operate at the knee point of the magnetization curve [1]. Therefore, some degree of magnetic saturation is present almost in every induction motor application.

Magnetic saturation is a complex phenomenon extensively studied by FEM (see, for example, [21]). For the purpose of modeling of an induction motor by its equivalent electrical circuit, it is typical to neglect leakage path saturation and to describe the teeth and core yoke saturation by a single main flux saturation characteristic [19].

We illustrate the difference between non-saturated and saturated induction motor models by the corresponding voltage equations in a general reference frame, using stator and rotor currents as state variables [19]. The non-saturated induction motor model is given by (1) and the saturated induction motor model is given by (2). The nomenclature for equations (1) and (2) appears below.

With regard to equation (1), R_s , R_r are stator and rotor resistances, respectively; L_m , L_s , L_r , L_{ls} , L_{lr} are magnetizing, stator, rotor, leakage stator, leakage rotor inductances, respectively, and $L_s = L_m + L_{ls}$, $L_r = L_m + L_{lr}$; ω_g , ω_r are angular frequencies of the frame and the rotor, respectively, and slip frequency is given by $\omega_{sl} = \omega_g - \omega_r$. Further, u is voltage; i is current; indexes x , y stand for the two reference frame axes; indexes s , r stand for stator and rotor; and $p = d/dt$.

Additionally, with regard to equation (2), $L_{sx} = L_s + \Delta L_{mx}$, $L_{sy} = L_s + \Delta L_{my}$, $L_{rx} = L_r + \Delta L_{mx}$, $L_{ry} = L_r + \Delta L_{my}$, where $\Delta L_{mx} = \Delta L_m \cos^2(\rho - \theta_g)$, $\Delta L_{my} = \Delta L_m \sin^2(\rho_m - \theta_g)$; $L_{xy} = \frac{1}{2} \Delta L_m \sin 2(\rho_m - \theta_g)$ is cross-saturation inductance; $\Delta L_m = L - L_m$ is the difference between dynamic $L = d|\bar{\psi}_m|/d|\bar{i}_m|$ and static $L_m = |\bar{\psi}_m|/|\bar{i}_m|$ magnetizing inductances.

Comparing (1) and (2), one can see the following consequences of magnetic saturation for the motor model:

- Additional cross-saturation terms (L_{xy}) appear between x and y axes in both stator and rotor currents;
- Additional magnetizing inductance terms are present (ΔL_{mx} , ΔL_{my}) which vary depending on the frame angle (θ_g) compared to the main flux angle (ρ_m);
- Static magnetizing inductance ($L_m = |\bar{\psi}_m|/|\bar{i}_m|$) is represented by its saturated values;
- Dynamic magnetizing inductance ($L = d|\bar{\psi}_m|/d|\bar{i}_m|$) is considered as opposed to the static magnetizing inductance.

Cross-saturation was the subject of extensive studies in 1980s-1990s. It was found that selection of state variables in the induction motor model may have effect on the importance of considering cross-saturation. For example, in [9], [10] it was shown that using stator and rotor fluxes as state variables not only eliminates explicit cross-saturation terms in the model but also makes the motor model less sensitive to the consideration of the dynamic inductance L .

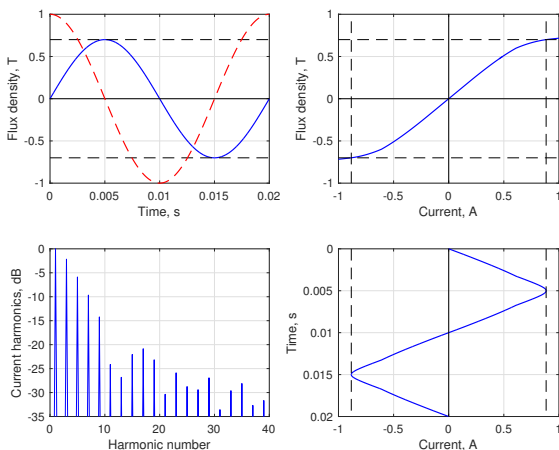


Fig. 1: Current harmonic distortion due to magnetic saturation

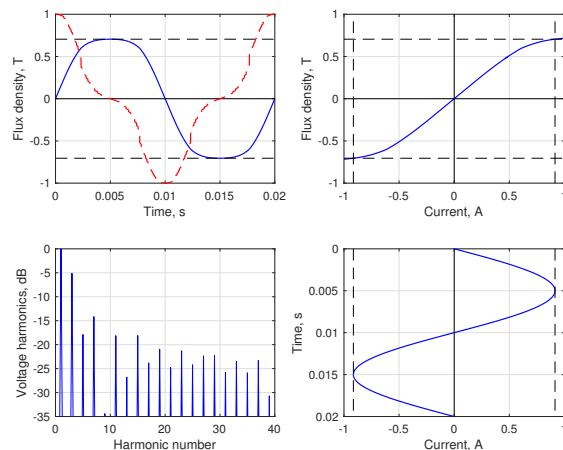


Fig. 2: Voltage harmonic distortion due to magnetic saturation

Controllers with new and Advanced Current Controllers, which serve two purposes. Firstly, they will offer improved tracking performance with respect to sinusoidal current references i_{α}^* and i_{β}^* , as compared to standard schemes. Secondly, they will eliminate (without feedforward compensation, such as Voltage Decoupler) the effects of any back-emf disturbances, including fundamental frequency components originating from rotation and harmonic components originating from magnetic saturation.

The outer control loops including Flux Controller and Speed Controller in Fig. 3 may remain unchanged. They may still benefit from the use of the ‘‘Flux and L_m Estimator’’ but the latter will only need to be updated at a very slow rate, corresponding to the low bandwidths of the outer loops. Alternatively, one of the known sensorless control methods with inclusion of saturation effects can be utilized, see, for example [7], [12].

Since the focus of this paper is the development of the advanced current control strategy, in Fig. 4 we show only the current control part of Fig. 3 together with a more detailed load model. Back-emf components are represented in Fig. 4 as voltage sources e_a, e_b, e_c . The diagram shown in Fig. 4 forms the basis of the study presented in this paper.

Provided that the disturbance voltages e_a, e_b, e_c are rejected by the control scheme, then current controls for α - and β -axis currents are decoupled. Each axis current is then given by a RL load model as:

$$\sigma L_s \frac{di(t)}{dt} + R_s i(t) = v(t) \quad (3)$$

where $\sigma = \frac{L_s L_r - L_m^2}{L_s L_r}$ is the leakage constant. Although L_s includes magnetizing inductance L_m , which can saturate, it can be shown that

$$\sigma L_s = \frac{L_s L_r - L_m^2}{L_r} = L_{ls} + \frac{L_{lr} L_m}{L_m + L_{lr}} \approx L_{ls} + L_{lr} \quad (4)$$

is practically not affected by saturation. This makes the RL model (3) practically linear. Back-emf voltages, on the other hand, depend on the main flux, which can saturate. Therefore, in the presence of magnetic saturation, voltages e_a, e_b, e_c will include both fundamental and odd-numbered harmonic components. More details on saturation modeling for simulation purpose is presented in section III.

We recall that PWM, by using different voltages from a limited set in one modulation cycle, very closely approximates a constant voltage of a desired magnitude. A well-known solution of equation (3) at the end of interval Δ , if a constant voltage $V = V(0)$ is applied for the entire interval Δ , is given by:

$$i(\Delta) = i(0)e^{-\frac{\Delta}{\tau_p}} + \frac{1}{R_s} V(0) \left(1 - e^{-\frac{\Delta}{\tau_p}}\right) \quad (5)$$

where $i(0)$ and $i(\Delta)$ are current at the beginning and at the end of interval Δ , respectively; and $\tau_p = L/R$ is the plant time constant.

This can be written in the following discrete form

$$(1 - az^{-1})i(z) = bz^{-1}v(z) \quad (6)$$

where $a = e^{-\frac{\Delta}{\tau_p}}$; $b = \frac{1}{R} \left(1 - e^{-\frac{\Delta}{\tau_p}}\right)$; $\tau_p = \sigma L_s / R_s$ and z^{-1} is the standard shift operator.

Model described by (6) will be used in the paper for the control design. Note that no knowledge about the saturation model will be required, except for knowing at which frequencies the saturation harmonics will occur. The control of the two orthogonal axes currents (i_{α} and i_{β}) will be implemented as two identical SISO systems.

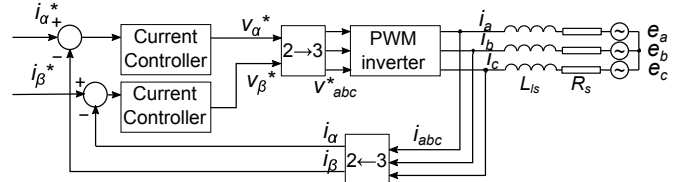


Fig. 4: Current control part of the proposed RFOC scheme

The layout of the remainder of the paper is as follows. In section II, theoretical basis for the proposed advanced control scheme is developed, based on horizon 1 MPC approach. In Section III the proposed control architecture is applied to the model of a saturated three phase induction motor. Extensive simulation results illustrate the tracking and harmonic performance of the proposed scheme. Section IV addresses various implementation aspects of the proposed scheme which results in a robust and resource-efficient implementation. Section IV also includes and discusses experimental results. Section V summarizes the main findings and conclusions of the paper.

II. THEORETICAL DEVELOPMENT OF THE PROPOSED CONTROL SCHEME

A. Polynomial Form of Linear Steady State Kalman Filter

The theory behind the proposed control scheme comes down to using a polynomial form of linear steady state Kalman Filter. Consider the following linear system having Gaussian white noise and periodic disturbance:

$$x_{k+1} = A_o x_k + B_o u_k + n_k \quad (7)$$

$$d_{k+1} = A_d d_k + \omega_k \quad (8)$$

$$y'_k = C_o x_k + C_d d_k + \nu_k \quad (9)$$

where x, u and y are state, input and output vectors, respectively; n, ω and ν are Gaussian white noise sequences; d is periodic disturbance; A_o, A_d, C_o, C_d and B_o are matrices of appropriate dimensions.

For example, if the plant model (6) is assumed then $A_o = a$; $B_o = b$. If disturbance at a single fundamental frequency ω_o is assumed then

$$A_d = \begin{bmatrix} 0 & 1 \\ -1 & 2 \cos(\omega_o \Delta) \end{bmatrix} \quad (10)$$

Given the model (7) to (9), the corresponding steady state Kalman filter takes the form:

$$\hat{x}_{k+1} = A_o \hat{x}_k + B_o u_k + J_o \left(y_k - C_o \hat{x}_k - C_d \hat{d}_k \right) \quad (11)$$

$$\hat{d}_{k+1} = A_d \hat{d}_k + J_d \left(y_k - C_o \hat{x}_k - C_d \hat{d}_k \right) \quad (12)$$

Using the above filter, the system output can be expressed in innovation form as

$$y'_{k+1} = C_o \hat{x}_k + C_d \hat{d}_k + \varepsilon_k \quad (13)$$

where ε_k is a white noise sequence.

It was shown in [4] that the innovation model (13) can be written in polynomial form as:

$$A(z)D(z)y'_k = B(z)D(z)u_k + C(z)\varepsilon_k \quad (14)$$

where

$$\frac{B(z)}{A(z)} = C_o (zI - A_o)^{-1} B_o \quad (15)$$

$$A(z) = \det(zI - A_o) \quad (16)$$

$$D(z) = \det(zI - A_d) \quad (17)$$

$$C(z) = \det \begin{bmatrix} zI - A_o + J_o C_d & J_o C_d \\ J_d C_o & zI - A_d + J_d C_d \end{bmatrix} \quad (18)$$

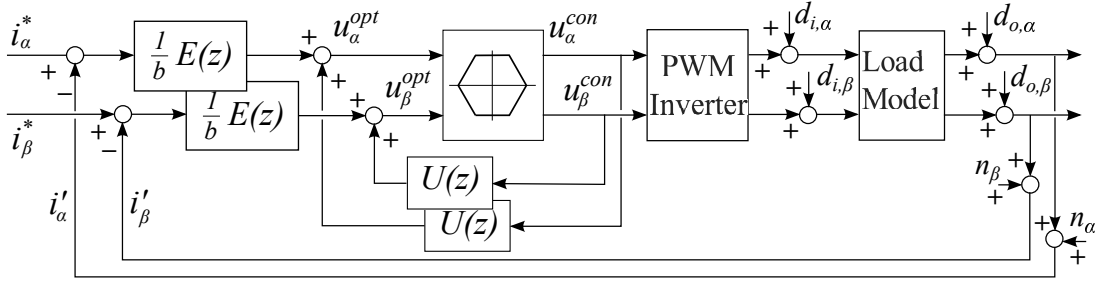


Fig. 5: Optimal current control rejecting errors at a single frequency ω_o

and z denotes shift operator.

As an example, say that the disturbance $C_d d_k$ is a single frequency disturbance at frequency ω_o , then

$$D(z) = 1 - 2 \cos(\omega_o \Delta) z^{-1} + z^{-2} \quad (19)$$

where Δ is the sampling period.

Note that $\{y_k^*\}$ can be converted to an output disturbance by defining the tracking error as

$$y_k = y_k' - y_k^* \quad (20)$$

Then the model (14) can be expressed in terms of the tracking error as

$$A(z)D(z)y_k = B(z)D(z)u_k + C(z)\varepsilon_k \quad (21)$$

where $D(z)$ now includes the model for both disturbance and the signal to be tracked.

Now, the objective is to bring the predicted output \hat{y}_{k+1}' to a desired value $\{y_k^*\}$. This is equivalent to minimizing a cost function given by:

$$J_k = \hat{y}_{k+1}'^2 \quad (22)$$

where \hat{y}_{k+1}' is predicted one step ahead tracking error.

B. MPC with disturbance rejection at a single frequency

We will now further develop the polynomial form (21) of the innovation model to determine the optimal control law in the sense of minimization of the cost function (21). Note that the control based on (a) predicting the plant output according to a given model and (b) minimizing a cost function is, essentially, MPC. In our case, MPC will be applied at the stage of development of the control law and will be implicitly present in the resulting control structure. This is different from conventional MPC applications in power electronics where model prediction and cost function minimization are performed explicitly in each control cycle [16].

The design of the optimal control law in the most general form was presented in [13]. In this paper we perform such design for a particular case where the current reference and the disturbance have the form of sinusoidal signals at the fundamental frequency. This is the most relevant case for the purpose of improving the tracking performance. Following this, we extend the design of the optimal controller to eliminating disturbances at multiple frequencies. This way, both tracking errors and harmonic distortion of the output current caused by magnetic saturation will be eliminated.

In case of both disturbance and reference being sinusoidal signals at the fundamental frequency ω_o , the model of the system is described by:

$$x_{k+1} = ax_k + bu_k + n_k \quad (23)$$

$$d_{k+1}^1 = d_k^2 + w_k^1 \quad (24)$$

$$d_{k+1}^2 = -d_k^1 + 2 \cos(\omega_o \Delta) d_k^2 + w_k^2 \quad (25)$$

$$y_k' = x_k + d_k^1 + \nu_k \quad (26)$$

where d^1 and d^2 are the two state variables describing output disturbance; w^1 and w^2 are the respective white noise sequences. Then the polynomial form of the corresponding innovation model, expressed in terms of the tracking error, will be given by:

$$A(z)D(z)y_k = B(z)D(z)u_k + C(z)\varepsilon_k \quad (27)$$

where $A(z) = z - a$; $B(z) = b$; $D(z) = z^2 - 2 \cos(\omega_o \Delta) z + 1$ and

$$C(z) = \det \begin{bmatrix} z - a + J_o & J_o & 0 \\ J_{d1} & z + J_{d1} & -1 \\ J_{d2} & 1 + J_{d2} & z - 2 \cos(\omega_o \Delta) \end{bmatrix}$$

where J_o , J_{d1} , J_{d2} are Kalman Filter gains. These gains can be determined, for example, by finding a steady state solution of the Riccati equation. Unfortunately, these gains depend on statistical properties of the noises n_k , w_k^1 , w_k^2 and ν_k in the model (23)-(26), which are not always known. Therefore, different choices of the Kalman Filter gains are possible, which deserves a separate study. In this paper we make use of one particular choice of J_o , J_{d1} , J_{d2} resulting in the following expression for $C(z)$:

$$C(z) = (z - a) (z^2 - 2\gamma \cos(\omega_o \Delta) z + \gamma^2) \quad (28)$$

where $\gamma < 1$. The reason of this selection is its simplicity, agreement with the intuitive understanding about the expected control action and agreement with the previous studies performed by the authors in [14]. It will be shown later in this paper that using $C(z)$ given by (28) results in noise sensitivity functions proportional to:

$$S(z) = \frac{1 - 2 \cos(\omega_o \Delta) z^{-1} + z^{-2}}{1 - 2\gamma \cos(\omega_o \Delta) z^{-1} + \gamma^2 z^{-2}} \quad (29)$$

Numerator of the transfer function (29) equals zero at the fundamental frequency $\pm\omega_o$ thus eliminating any error at this frequency. Denominator of the transfer function (29) cancels the effect of the numerator everywhere except around the fundamental frequency $\pm\omega_o$ thus ensuring that the error elimination is selective. The single tunable parameter γ determines the rejection bandwidth around $\pm\omega_o$. From practical considerations, $0.9 < \gamma < 0.99$.

We now assume $C(z)$ given by (28) and proceed with the design of the optimal controller. We divide both sides of equation (27) by polynomial $C(z)$ resulting in:

$$\frac{1 - 2 \cos(\omega_o \Delta) z^{-1} + z^{-2}}{1 - 2\gamma \cos(\omega_o \Delta) z^{-1} + \gamma^2 z^{-2}} y_k = b \frac{z^{-1} (1 - 2 \cos(\omega_o \Delta) z^{-1} + z^{-2})}{(1 - az^{-1})(1 - 2\gamma \cos(\omega_o \Delta) z^{-1} + \gamma^2 z^{-2})} u_k + \varepsilon_k \quad (30)$$

where z^{-1} denotes shift operator. We then factor transfer function on the left hand side of (12) which results in:

$$y_k = \frac{2(1-\gamma) \cos(\omega_o \Delta) z^{-1} - (1-\gamma^2) z^{-2}}{1 - 2\gamma \cos(\omega_o \Delta) z^{-1} + \gamma^2 z^{-2}} y_k + b \frac{z^{-1} (1 - 2 \cos(\omega_o \Delta) z^{-1} + z^{-2})}{(1 - az^{-1})(1 - 2\gamma \cos(\omega_o \Delta) z^{-1} + \gamma^2 z^{-2})} u_k + \varepsilon_k \quad (31)$$

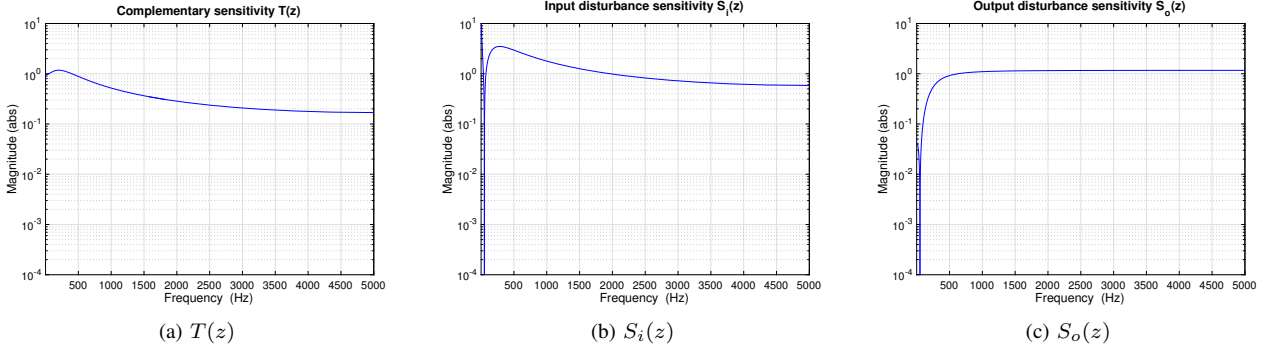


Fig. 6: Sensitivity functions of the control structure with one rejection frequency

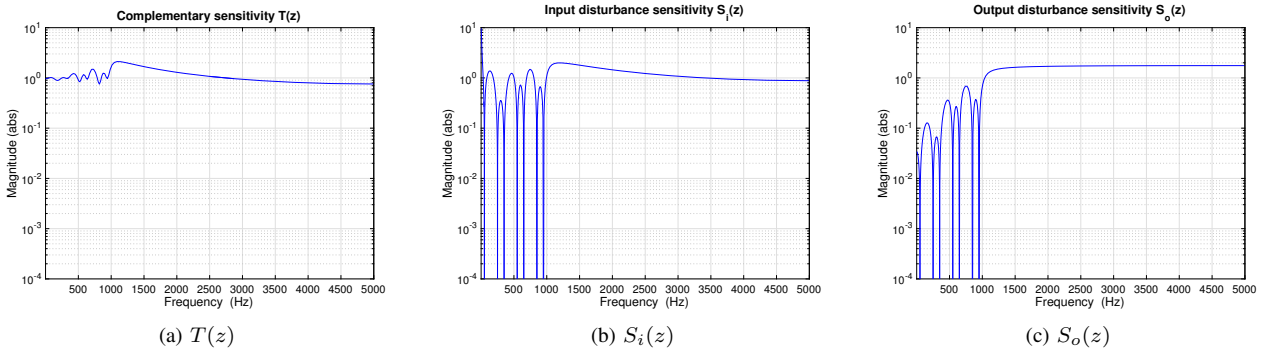


Fig. 7: Sensitivity functions of the control structure with seven rejection frequencies

Note that the right hand side of equation (31) depends only on the past values of y_k and u_k . We now form a one-step ahead prediction of y_k as:

$$\hat{y}_{k+1} = \frac{2(1-\gamma) \cos(\omega_o \Delta) - (1-\gamma^2)z^{-1}}{1-2\gamma \cos(\omega_o \Delta)z^{-1} + \gamma^2 z^{-2}} y_k + \frac{b(1-az^{-1})(1-2\gamma \cos(\omega_o \Delta)z^{-1} + \gamma^2 z^{-2})}{(1-az^{-1})(1-2\gamma \cos(\omega_o \Delta)z^{-1} + \gamma^2 z^{-2})} u_k \quad (32)$$

The future noise ε_k is unpredictable, hence is not present in (32). At this stage we apply cost function (22) corresponding to the tracking error squared. Clearly, its minimum value is zero. This will correspond to such a control law u_k which brings the right hand side of (32) to zero. We then factor the second term of (32) to separate the latest control law u_k , which is yet to be determined, from its past values u_{k-1} , u_{k-2} , ..., which are known but cannot be changed. Using the tracking error expression (20), this results in:

$$u_k^{opt} = \frac{1}{b} (y_k^* - y_k) \frac{\varepsilon_1 - \varepsilon_2 z^{-1}}{1 - 2\gamma \cos(\omega_o \Delta) z^{-1} + \gamma^2 z^{-2}} - \frac{(a - \varepsilon_1) z^{-1} - (2a\gamma \cos(\omega_o \Delta) - \varepsilon_2) z^{-2} + a\gamma^2 z^{-3}}{(1 - az^{-1})(1 - 2\gamma \cos(\omega_o \Delta) z^{-1} + \gamma^2 z^{-2})} u_k \quad (33)$$

where $\varepsilon_1 = 2(1 - \gamma) \cos(\omega_o \Delta)$ and $\varepsilon_2 = 1 - \gamma^2$. This is indeed the optimal unconstrained control law u_k^{opt} which brings the chosen cost function (the tracking error) to its minimal (zero) value. If the control law has to be constrained, for example, by a hexagon on $\alpha\beta$ plane for a 2-level PWM inverter, then we choose the control law nearest to u_k^{opt} :

$$u_k^{con} = [\text{Nearest } \bar{u} \in U \text{ to } u_k^{opt}] \quad (34)$$

The resulting optimal (in MPC sense) control structure is

shown in Fig. 5 where

$$E(z) = z \left(1 - \frac{1 - 2 \cos(\omega_o \Delta) z^{-1} + z^{-2}}{1 - 2\gamma \cos(\omega_o \Delta) z^{-1} + \gamma^2 z^{-2}} \right) \\ U(z) = 1 - \frac{1 - 2 \cos(\omega_o \Delta) z^{-1} + z^{-2}}{(1 - az^{-1})(1 - 2\gamma \cos(\omega_o \Delta) z^{-1} + \gamma^2 z^{-2})} \quad (35)$$

As seen from Fig. 5 the optimal control is applied to each of the two controlled currents (i_α and i_β) independently. The shared constraint block corresponds to the hexagonal limits in $\alpha\beta$ - frame. If an unconstrained voltage vector $u_{\alpha\beta}^{opt}$ lies outside the hexagon then it is limited to the vector $u_{\alpha\beta}^{con}$ which belongs to the hexagon boundary and has the same direction as $u_{\alpha\beta}^{opt}$.

The control structure shown Fig. 5 is inherently anti-windup, since the actual (saturated) control $u_{\alpha\beta}^{con}$ is fed back to become a part of the $u_{\alpha\beta}^{opt}$ calculation. This is exactly the way that the control needs to be implemented. However, to get a better insight into the nature of the designed controller, we neglect the saturation block and transform the combination of the $\frac{1}{b}E(z)$ and $U(z)$ blocks into one equivalent transfer function as:

$$\frac{\frac{1}{b}E(z)}{1 - U(z)} = \frac{1}{b} (1 - az^{-1}) \frac{\varepsilon_1 - \varepsilon_2 z^{-1}}{1 - 2 \cos(\omega_o \Delta) z^{-1} + z^{-2}} \quad (36)$$

Using the plant model (6) and the controller transfer function (36), we can determine the closed loop transfer function of the system as:

$$T(z) = 1 - \frac{1 - 2 \cos(\omega_o \Delta) z^{-1} + z^{-2}}{1 - 2\gamma \cos(\omega_o \Delta) z^{-1} + \gamma^2 z^{-2}} \quad (37)$$

The transfer function $T(z)$ is applied to the current references $i^*(k)$ and the current measurement noises $n(k)$ in Fig. 5.

Sensitivity function with respect to the input noise (dis-

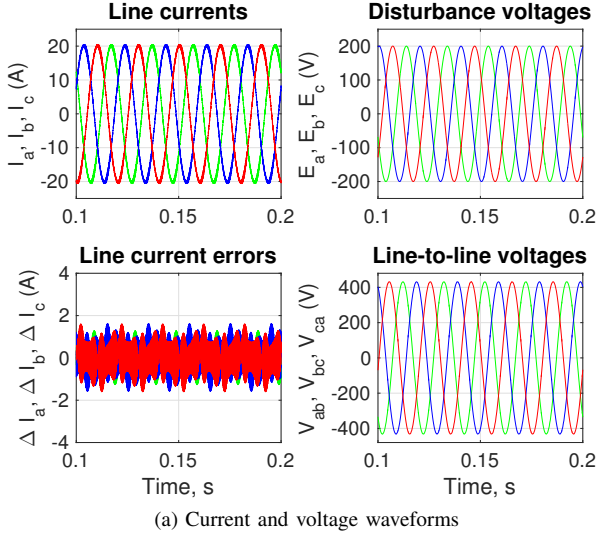


Fig. 8: Single frequency disturbance, standard PI controller

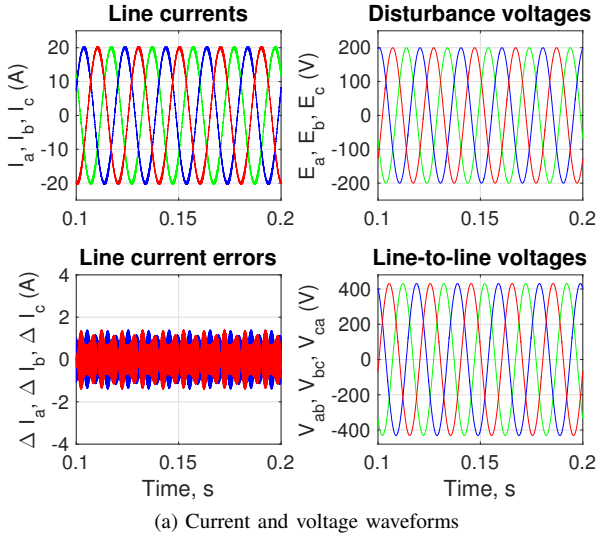


Fig. 9: Single frequency disturbance, proposed controller tuned to single frequency

turbances d_i in Fig. 5) is given by:

$$S_i(z) = \frac{bz^{-1}}{1-az^{-1}} \frac{1-2\cos(\omega_o\Delta)z^{-1}+z^{-2}}{1-2\gamma\cos(\omega_o\Delta)z^{-1}+\gamma^2z^{-2}} \quad (38)$$

The input noise includes voltage disturbances, for example, back-emf disturbances and voltage quantization noise due to PWM action.

Sensitivity function with respect to the output noise (d_o in Fig. 5) is given by:

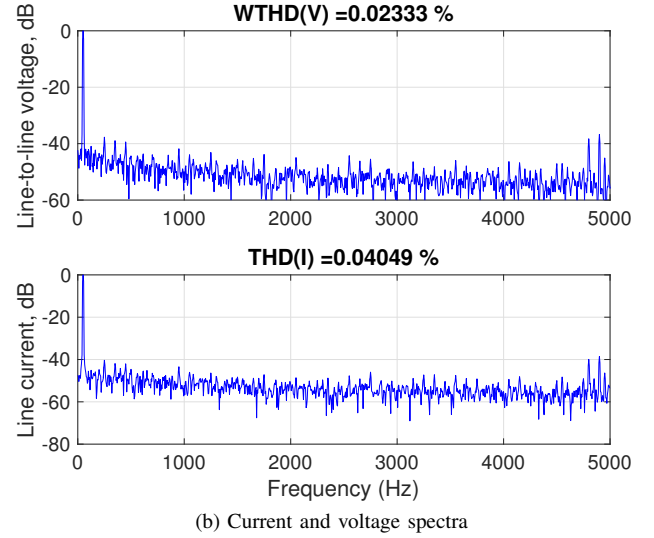
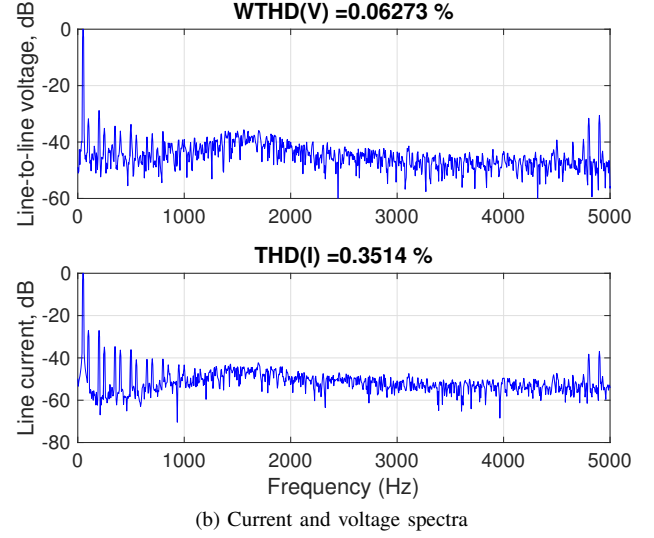
$$S_o(z) = \frac{1-2\cos(\omega_o\Delta)z^{-1}+z^{-2}}{1-2\gamma\cos(\omega_o\Delta)z^{-1}+\gamma^2z^{-2}} \quad (39)$$

The output noise includes current disturbances, for example, those related to switching delays. Current ripple due to PWM action and current harmonics due to saturation can be also seen as output disturbances if convenient.

The magnitude Bode plots of the three above sensitivity functions appear in Fig. 6: $T(z)$ - in Fig. 6a; $S_i(z)$ - in Fig. 6b; and $S_o(z)$ - in Fig. 6c. The resulting expression for the output current is:

$$i_{\alpha\beta} = T(z)i_{\alpha\beta}^* + S_i(z)d_{i,\alpha\beta} + S_o(z)d_{o,\alpha\beta} - T(z)n_{\alpha\beta} \quad (40)$$

Note that at the fundamental frequency (50 Hz in the example given) $T(z) = 1$ and $S_i(z) = S_o(z) = 0$. Therefore, the



reference at 50 Hz is tracked with gain 1, and input and output disturbances at 50 Hz are fully rejected by applying gains 0, as expected.

C. MPC with disturbance rejection at multiple frequencies

The principle described in section II-B can be now extended to multiple frequencies. The polynomial form of the innovation model (27) will have the following definitions of the polynomials: $A(z) = z - a$; $B(z) = b$; $D(z) = \prod_i [z^2 - 2\cos(\omega_i\Delta)z + 1]$, where ω_i ($i = 1, 2, \dots$) are the frequencies at which disturbances are to be rejected. A particular selection of the Kalman Filter gains results in the following definition of the polynomial $C(z)$:

$$C(z) = (z - a) \prod_i [z^2 - 2\gamma_i \cos(\omega_i\Delta)z + \gamma_i^2] \quad (41)$$

where γ_i are the tunable parameters ($0.9 < \gamma_i < 0.99$), one per each frequency of rejection. Then, following the design steps similar to (30)-(32), the optimal unconstrained control law results:

$$u_k^{opt} = \frac{1}{b} \left(y_k^* - y_k' \right) E(z) + U(z)u_k \quad (42)$$

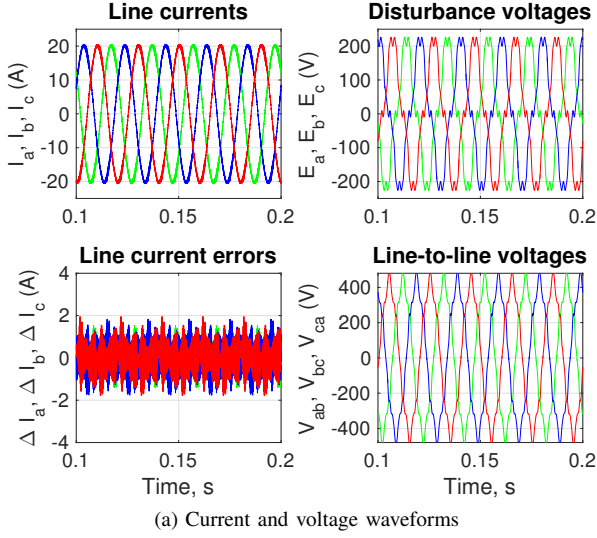


Fig. 10: Multiple frequency disturbance, standard PI controller

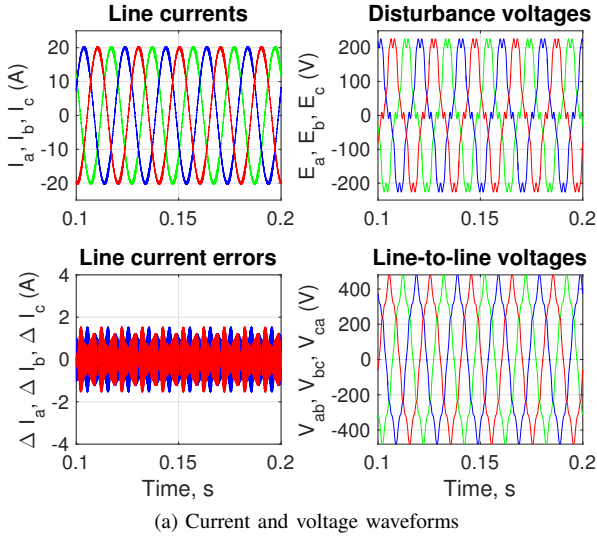


Fig. 11: Multiple frequency disturbance, proposed controller tuned to multiple frequencies

where

$$E(z) = z \left\{ 1 - \frac{\prod_i [1 - 2 \cos(\omega_i \Delta) z^{-1} + z^2]}{\prod_i [1 - 2\gamma_i \cos(\omega_i \Delta) z^{-1} + \gamma_i^2 z^2]} \right\}$$

$$U(z) = 1 - \frac{\prod_i [1 - 2 \cos(\omega_i \Delta) z^{-1} + z^2]}{(1 - az^{-1}) \prod_i [1 - 2\gamma_i \cos(\omega_i \Delta) z^{-1} + \gamma_i^2 z^2]} \quad (43)$$

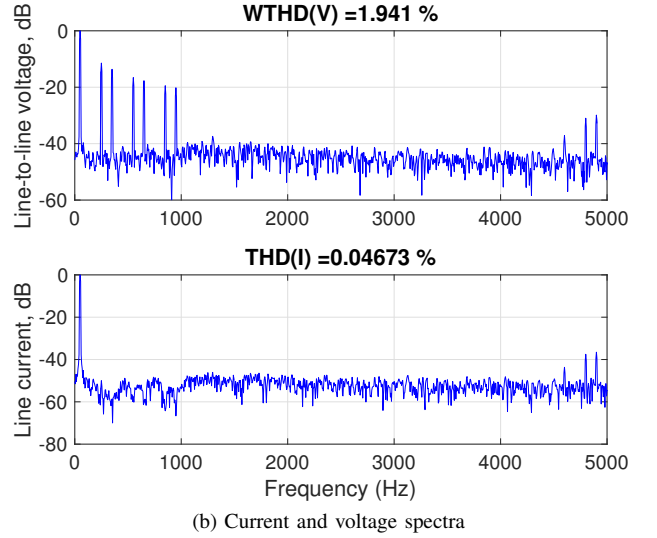
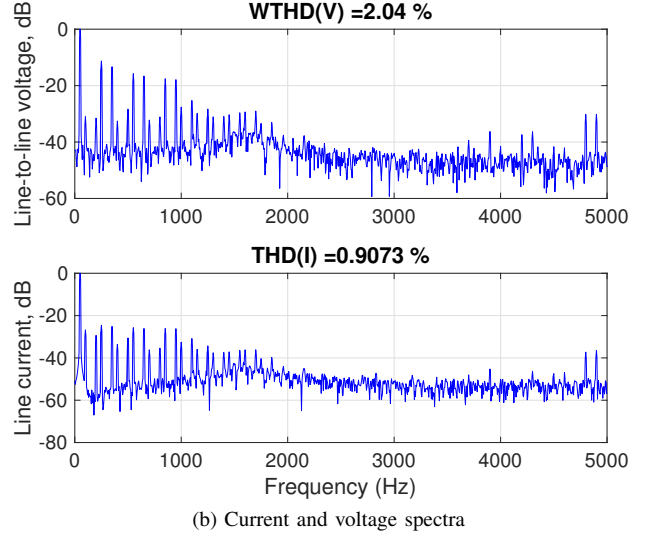
For the constrained control law, u_k^{con} nearest to u_k^{opt} from the available control set needs to be chosen. The same control structure of Fig. 5 applies, with the new definitions of $E(z)$ and $U(z)$ by (43). The new sensitivity functions are now given by:

$$T(z) = 1 - \prod_i \frac{1 - 2 \cos(\omega_i \Delta) z^{-1} + z^{-2}}{1 - 2\gamma_i \cos(\omega_i \Delta) z^{-1} + \gamma_i^2 z^{-2}}$$

$$S_o(z) = \prod_i \frac{1 - 2 \cos(\omega_i \Delta) z^{-1} + z^{-2}}{1 - 2\gamma_i \cos(\omega_i \Delta) z^{-1} + \gamma_i^2 z^{-2}} \quad (44)$$

$$S_i(z) = \frac{bz^{-1}}{1 - az^{-1}} \prod_i \frac{1 - 2 \cos(\omega_i \Delta) z^{-1} + z^{-2}}{1 - 2\gamma_i \cos(\omega_i \Delta) z^{-1} + \gamma_i^2 z^{-2}}$$

Note that the previously developed optimal control with single frequency of rejection is a special case of the optimal control with multiple frequencies of rejection where $i = 1$; $\omega_1 = \omega_0$ and $\gamma_1 = \gamma$.



As an illustration we chose seven frequencies ω_i as: the fundamental frequency ω_0 and its harmonics number 5, 7, 11, 13, 17 and 19. The corresponding magnitude Bode plots of the three above sensitivity functions appear in Fig. 7: $T(z)$ - in Fig. 7a; $S_i(z)$ - in Fig. 7b; and $S_o(z)$ - in Fig. 7c. Note that at any of the frequencies ω_i the disturbances are fully rejected, since $S_i(z) = S_o(z) = 0$. Provided that the reference corresponds to ω_0 , then $T(z = e^{j\omega_0}) = 1$ and hence a perfect reference tracking is also achieved.

III. APPLICATION TO A SATURATED INDUCTION MOTOR IN SIMULATION

The proposed control structure shown in Fig.5 and described in sections II-B and II-C is now applied to a model of an induction motor in Matlab environment. Parameters of the induction motor and the inverter are given in Table I. These parameters correspond to a standard 11kW 415V 20A induction motor.

First, we simulate the performance of current control applied to an unsaturated motor. This is achieved by implementing the current control scheme shown in Fig. 4 with back-emf voltages of pure sinusoidal shape. Simulation results shown in Fig. 8 correspond to using a standard PI controller for both α - and β - axis current control. Tracking

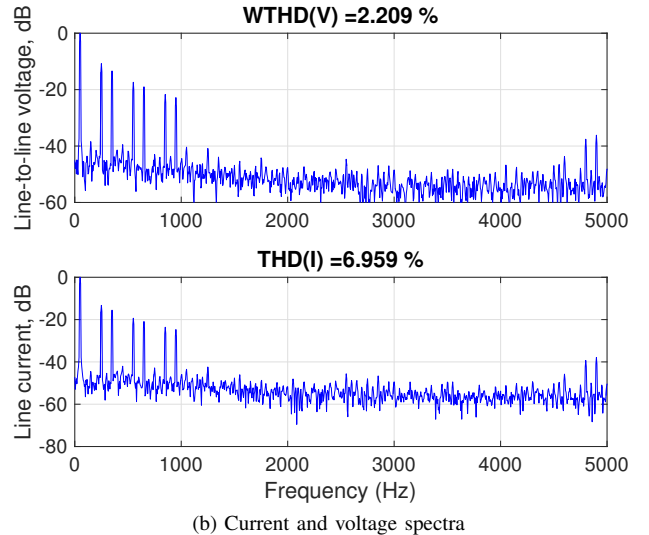
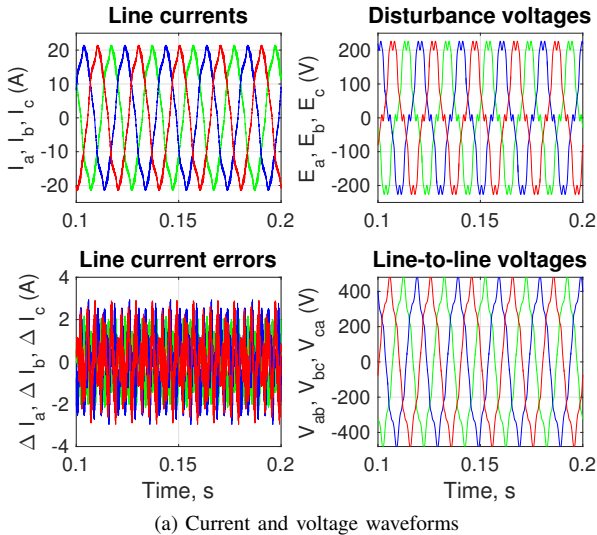


Fig. 12: Multiple frequency disturbance, standard PR controller

Motor parameter	Value	Inverter parameter	Value
Stator resistance, Ω	0.146	DC-link, V	600
Leakage inductance, mH	4.2	Sampling f_s , Hz	5000
Magnetizing inductance, mH	86.6	Modulation scheme (SVM)	Symmetrical asynchronous
Connection	Star	Fundamental f_o , Hz	50
Back-emf at rated speed, V_{peak}	200		

Table I: Parameters of motor and inverter

error in this case is 0.76%, which is acceptable. However, a number of harmonics exist in the line current, and overall current THD is 0.35%. This may be considered acceptable.

Now compare the performance of the PI controller to the performance of the proposed controller designed to reject single frequency disturbances, as described in section II-B. Simulation results presented in Fig. 9 show much smaller tracking error which amounts only 0.05%. The harmonic components in the line current are well below -40 dB, with overall current THD of only 0.04%.

In the second case, we simulate current control of a saturated induction motor. This is achieved by injecting distorted back-emf voltages in the current control scheme of Fig. 4. Fig. 10 shows simulation results for the PI controller. While its tracking performance with respect to the fundamental frequency is still good (tracking error 0.76%), a significant degradation of the harmonic performance is evident. This is the consequence of the fact that low frequency voltage harmonics produce corresponding current harmonics with very little attenuation. Weighted total harmonic distortion (WTHD) of line-to-line voltage is approximately 2% and THD of line current is 0.9%.

Fig. 11 presents corresponding simulation results for the proposed current control scheme designed to reject multiple frequencies, as described in section II-C. Tracking performance continues to be excellent (tracking error 0.05%) due to the inclusion of the fundamental frequency into the range of the rejection frequencies. Note that only errors at these frequencies are rejected, i.e. the tracking errors but not the fundamental reference. While the voltage waveform is still significantly distorted (WTHD \approx 2%), low frequency harmonics are successfully rejected in the current spectrum, and THD of the line current is below 0.05%.

Finally, one may wish to compare the performance of the proposed current control scheme to another standard current controller, namely, proportional - resonant, or PR controller. This case is illustrated in Fig. 12. The tracking performance in this case will be approximately the same as with the proposed controller (0.05% tracking error) but the

harmonic performance (THD \approx 7%) is much worse than with the proposed controller or even with the PI controller. This is because the additional harmonics are not attenuated at all by the PR controller scheme.

It can be concluded that the proposed current control scheme successfully achieves both improved tracking error and improved harmonic performance, as compared to the standard control schemes.

IV. IMPLEMENTATION ASPECTS AND EXPERIMENTAL RESULTS

High order filters described by (35) need a thoughtful implementation. Two important aspects of such an implementation are particularly worth mentioning. These are: parallel second order sections and delta-form digital filter as opposed to shift-form. To illustrate the first aspect, we consider a case where rejection is achieved at n frequencies. Digital implementation of the filter $E(z)$ from Fig. 5 will look as follows:

$$y(k) = a_1 y(k-1) - a_2 y(k-2) + \dots - a_{2n} y(k-2n) + b_0 x(k) - b_1 x(k-1) + \dots - b_{2n-1} x(k-(2n-1)) \quad (45)$$

where $x(k)$ and $y(k)$ are filter input and output, respectively, and all coefficients a_i , b_i are positive.

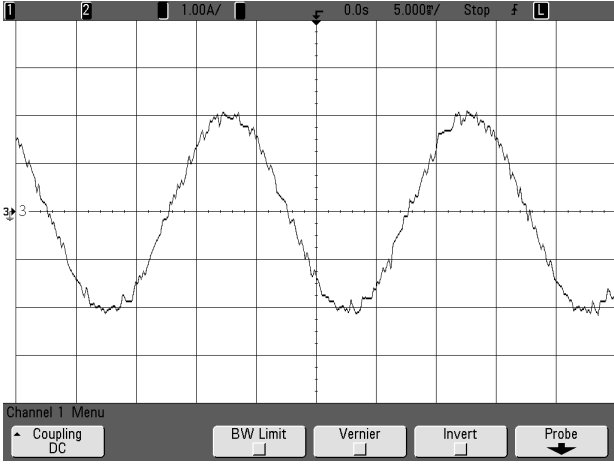
One can see from (45) that output $y(k)$ is obtained by adding a long chain of weighted previous outputs and inputs of the filter. Note that, due to fast sampling rate, previous outputs $y(k-1) \dots y(k-2n)$ may have values that are very close to each other. The sum of the weights applied to $y(k-1) \dots y(k-2n)$ is close to zero. The same is true for the previous inputs $x(k-1) \dots x(k-(2n-1))$ and their weights. It follows that the result will depend on how accurately the close values cancel each other, and will be very sensitive to numeric errors.

To avoid that, exactly the same filter can be implemented as a parallel connection of three second order filters as in:

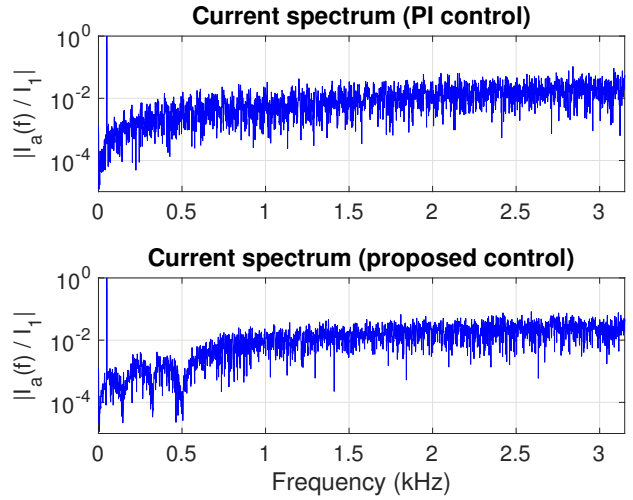
$$y(k) = y_1(k) + \dots + y_n(k) \quad (46)$$

where each of the second order filter outputs has the form: $y_i(k) = a_{1i} y_i(k-1) - a_{2i} y_i(k-2) + b_{0i} x(k) - b_{1i} x(k-1)$.

One can see that each of the simple second order filters is driven by its own past outputs and the common input. Each one of them has a ‘‘short memory’’ and does not rely on cancellation of close numeric values. Filter coefficients



(a) Current waveform (proposed control)



(b) Current spectra (top: PI control; bottom: proposed control)

Fig. 13: Experimental results for 3rd, 7th and 11th harmonics rejection

can be obtained offline, with high accuracy, using standard mathematical functions of partial fraction decomposition (e.g. *residue* function in Matlab) and then stored in the memory of a controller.

The second very important aspect of robust filter design is using delta-form rather than shift-form digital filter implementations. We illustrate this on a very simple example of a first order low pass filter, with gain 1 at zero frequency, which continuous time and discrete time transfer functions are given next to each other as:

$$G(s) = \frac{1/T}{s + 1/T}; \quad G(z) = \frac{(1 - e^{-\Delta/T}) z^{-1}}{1 - e^{-\Delta/T} z^{-1}} \quad (47)$$

where $\omega_c = 1/T$ is cutoff frequency and Δ is sampling period. Say, for simplicity, that $\omega_c = 2\pi$ rad/s (or 1 Hz) and sampling frequency is 10kHz. Then algorithmic implementation of such a digital filter will look like:

$$y(k) = 0.999372y(k-1) + 0.000628x(k-1) \quad (48)$$

The first coefficient in (48) is very close to 1, and the second coefficient - very close to zero. Say, due to numeric errors both terms of the right hand side of (48) are calculated with relative error $\pm 10^{-4}$.

In the extreme case of both terms having maximum negative errors this is equivalent to:

$$y(k) = 0.999272y(k-1) + 0.000528x(k-1) \quad (49)$$

which corresponds to a filter with zero frequency gain 0.725 (instead of 1) and cutoff frequency 1.16Hz (instead of 1Hz). In the opposite case of both terms having maximum positive errors then we have a filter with zero frequency gain 1.379 and cutoff frequency 0.84Hz. If the first term in (48) has an error approaching $+6.3 \times 10^{-4}$ then the filter is unstable.

This example illustrates that both gains and frequencies to which filters are tuned, become severely affected by numeric errors if filters are implemented in the shift form, as in (45), (46) and (48). This can easily lead to instability. The alternative is known as delta-form of digital transfer functions (see [5]). The delta form of the digital filter (48) will look like:

$$y(k) = y(k-1) + 0.000628(x(k-1) - y(k-1)) \quad (50)$$

The larger part of the right hand side of (50) is the previous value $y(k-1)$ with coefficient 1, which will never be affected by numeric errors. The smaller part of the right hand side of (50) is a small coefficient multiplied by the

difference between past input and output, which rolls down to zero as the system approached steady state. Overwhelming advantages of delta-form implementation has been shown in [3]. Following the method explained in [3], we implemented each of the second order sections of a high-order digital filter as a modified canonic δ -filter.

Experimental results for the proposed current control scheme are shown in Fig. 13. The case illustrated in Fig. 13 corresponds to the rejection of three harmonic components in the current spectrum, namely, of the 3rd, 7th and 11th harmonics.

The current waveform for this case is shown in Fig. 13a and the corresponding spectrum - in Fig. 13b (bottom plot).

For comparison, the current spectrum obtained when using a standard PI controller is shown in Fig. 13b (top plot). One can observe the presence of almost every harmonic in this spectrum. This is due to magnetic saturation, phase unbalance and possibly other reasons.

Regardless of the the origin of the harmonics, they are successfully rejected by the proposed current control scheme, as follows from Fig. 13b (bottom plot). Moreover, the entire low frequency range of the current spectrum is pushed down to approximately 10^{-3} level. This means that, in practice, it is not necessary to design the current control to reject every undesirable harmonic component. It may be sufficient to reject only a few harmonics with a bonus of simultaneous attenuation of the adjacent harmonics.

V. CONCLUSIONS

The main contributions of the paper are the following:

- it has reviewed the mechanisms and effects of magnetic saturation, as well as control of a saturated induction motor;
- it has presented an approach to eliminate the effects of the magnetic saturation on tracking and harmonic performance of Field Oriented control of induction motors. The presented approach does not require an accurate knowledge of the saturated motor model and works well with a simplified (linear) motor model;
- it has developed MPC horizon 1 to designing control systems with superior tracking performance and simultaneous disturbance rejection at single or multiple frequencies;
- it has presented the structure and design details of an advanced current regulator based on the above

principles. This included implementation details such as robustness with respect to numeric errors.

- it has supported the discussion with extensive simulation results and preliminary experimental results.

- [21] K. Yamazaki. Comparison of induction motor characteristics calculated from electromagnetic field and equivalent circuit determined by 3d fem. *IEEE Transactions on Magnetics*, 36(4):1881–1885, July 2000.

REFERENCES

- [1] M. Bodson, O. Kiselychuk, and J. Wang. Comparison of two magnetic saturation models of induction machines. In *978-1-4673-4974-1/13*, pages 938–943, 2013.
- [2] X. Du, C. Sun, L. Guo, and Y. Zhou. Saturation harmonic effect of induction motor on aircraft power quality. In *2014 IEEE 9th Conference on Industrial Electronics and Applications (ICIEA)*, pages 2056–2060, 2014.
- [3] R.M. Goodall and B.J. Donoghue. Very high sample rate digital filters using the delta operator. *Circuits, Devices and Systems, IEE Proceedings*, 140(3):199–206, 1993.
- [4] G.C. Goodwin, D. S. Carrasco, and M. M. Seron. Predictive control: a historical perspective. *IJ of Robust and Nonlinear Control*, 22:1296–1313, 2012.
- [5] G.C. Goodwin, S.F. Graebe, and M.E. Salgado. *Control System Design*. Prentice Hall, 2001.
- [6] Y. Guan, Z.Q. Zhu, I. Afinowi, and J.C. Mipo. Influence of machine design parameters on flux-weakening performance of induction machine for electrical vehicle application. *Electrical Systems in Transportation, IET*, 5(1):43–52, 2015.
- [7] J. Holtz and H. Pan. Elimination of saturation effects in sensorless position-controlled induction motors. *Industry Applications, IEEE Transactions on*, 40(2):623–631, March/April 2004.
- [8] G. Joksimovic. Stator current harmonics in saturated cage and wound rotor induction motors. In *XIX International Conference on Electrical Machines - ICEM 2010*, pages 1–6, 2010.
- [9] E. Levi. A unified approach to main flux saturation modelling in d-q axis models of induction machines. *IEEE Transactions on Ene*, 10(3):455–461, September 1995.
- [10] E. Levi. Impact of cross-saturation on accuracy of saturated induction machine models. *IEEE Transactions on Energy Conversion*, 12(3):211–216, September 1997.
- [11] P. Ljusev, G. Stumberger, and D. Dolinar. Rotor flux linkage oriented control of induction motor with included magnetic saturation. *IEE Proceedings - Electric Power Applications*, 152(1):112–118, January 2005.
- [12] A. Makouf, M.E.H. Benbouzid, D. Diallo, and N.E. Bouguechal. A practical scheme for induction motor speed sensorless field-oriented control. *Energy Conversion, IEEE Transactions on*, 19(1):230–231, March 2004.
- [13] G. Mirzaeva, G. Goodwin, B. McGrath, C. Teixeira, and M. Rivera. A generalized MPC framework for the design and comparison of vsr current controllers. *IEEE Transactions on Industrial Electronics*, accepted for publ.:1–8, 2016.
- [14] G. Mirzaeva and G.C. Goodwin. Advanced noise shaping and filter design with feedback quantizer PWM. In *Industrial Technology (ICIT), 2013 IEEE International Conference on*, pages 469–474, 2013.
- [15] G. Mirzaeva, G.C. Goodwin, and B. McGrath. Optimal design of vsr current controllers based on MPC approach. In *International Symposium on Industrial Electronics (ISIE) 2015, Rio de Janeiro (Brazil)*, pages 1–6, 2015.
- [16] J. Rodríguez, M.P. Kazmierkowski, J.R. Espinoza, P. Zanchetta, H. Abu-Rub, H.A. Young, and C.A. Rojas. State of the art of finite control set model predictive control in power electronics. *Industrial Informatics, IEEE Transactions on*, 9(2):1003–1016, 2013.
- [17] F. Therrien, M. Chapariha, and J. Jatskevich. Constant-parameter voltage-behind-reactance induction machine model including main flux saturation. *IEEE Transactions on Energy Conversion*, 30(1):90–102, March 2015.
- [18] X. Tu, L.-A. Dessaint, R. Champagne, and K. Al-Haddad. Transient modeling of squirrel-cage induction machine considering air-gap flux saturation harmonics. *IEEE Transactions on Industrial Electronics*, 55(7):2798–2809, July 2008.
- [19] P. Vas. *Sensorless Vector and Direct Torque Control*. Oxford University Press, 2003.
- [20] P. Vas and M. Alakula. Field-oriented control of saturated induction machines. *Energy Conversion, IEEE Transactions on*, 5(1):218–224, March 1990.